Accepted Manuscript

A discontinuous Galerkin method for the mono-energetic Fokker–Planck equation based on a spherical interior penalty formulation

Aldo Hennink, Danny Lathouwers

PII: S0377-0427(17)30408-9
DOI: http://dx.doi.org/10.1016/j.cam.2017.08.019
Reference: CAM 11271

To appear in: *Journal of Computational and Applied Mathematics*

Received date : 16 February 2017
Revised date : 26 July 2017

Please cite this article as: A. Hennink, D. Lathouwers, A discontinuous Galerkin method for the mono-energetic Fokker–Planck equation based on a spherical interior penalty formulation, *Journal of Computational and Applied Mathematics* (2017), http://dx.doi.org/10.1016/j.cam.2017.08.019

A Discontinuous Galerkin Method for the Mono-Energetic Fokker-Planck Equation based on a Spherical Interior Penalty Formulation

Aldo Hennink[1*] and Danny Lathouwers[1]

[1]Department of Radiation Science and Technology, Delft University of Technology
[*]corresponding author (a.hennink@tudelft.nl; Mekelweg 15, 2629 JB Delft, The Netherlands)

July 26, 2017

Abstract

We present a new discretization of the mono-energetic Fokker-Planck equation. We build on previous work (Kophazi and Lathouwers, A space-angle DGFEM approach for the Boltzmann radiation transport equation with local angular refinement, j. of computational phys., 297:637-668, 2015) where we devised an angular discretization for the Boltzmann equation, allowing for both heterogeneous and anisotropic angular refinement. The angular discretization is based on a discontinuous finite element method on the unit sphere. Here we extend the methodology to include the effect of the Fokker-Planck scatter operator describing small angle particle scatter. We describe the construction of an interior penalty method on the sphere surface. Results are provided for a variety of test cases, ranging from purely angular to fully three-dimensional. The results show that the scheme can resolve highly forward-peaked flux distributions with forward-peaked scatter.

Keywords: discontinuous Galerkin, Fokker-Planck, particle transport, radiation transport, upwinding, interior penalty

1 Introduction

Charged particle radiation occurs in fields such as radiotherapy, plasma physics, and material sciences. To consider the effects of such radiation one needs an accurate description of how the particles interact with materials of interest such as human tissue.

The interactions of charged particles with the nuclei and the electrons of the material cause a variety of processes that are fundamentally different from those encountered with neutral particles such as photons and neutrons. Charged particle interactions are much more frequent and therefore lead to very large cross sections. Many of these interactions lead to either small deflections in the

direction of the particle with a negligible energy loss, or a small energy loss and a negligible deflection. Conversely, nuclear interactions can cause large deflections, transmutation or secondary particles to form [23]. Though the processes are quite different from neutral particles, the radiation field is accurately described by the linear Boltzmann equation with appropriate cross section data. The small deflection in Coulomb scatter means that highly forward-peaked scatter needs to be resolved. In many cases one can use the Fokker-Planck approximation, where the deflection angle tends to zero while the momentum transfer stays constant [21]. In this work, we will focus on the discretization of the angular part of the Fokker-Planck equation.

There are two computational approaches to solving the Boltzmann (or Fokker-Planck) equation: the Monte Carlo method and the deterministic method [18]. The Monte Carlo method is highly accurate both with respect to geometry and in simulating complex particle physics, but may be slow when complete distributions are of interest. The deterministic method is based on a discretization of the Boltzmann (Fokker-Planck) problem in space, angle and energy. Modern deterministic methods are well-equipped to handle complex geometries and are more efficient when one is interested in complete distributions [3].

The most commonly applied angular discretization is the method of discrete ordinates or S_N method. Morel [21] showed that standard S_N codes can perform charged particle transport calculations through careful manipulation of the cross sections used, so that state of the art neutral-particle tools can also be used for charged particle transport. Another method to handle highly forward-peaked scatter is the so-called extended-transport correction. There too the Legendre scatter cross sections are manipulated to mimic the physics of the problem [10]. The problem with the S_N method is that it cannot be anisotropically refined in angle, which is required for efficient solution methods in many practical problems, such as radiotherapy. Product quadratures (e.g. [22]) can focus on the solution close to a single direction (the pole of the sphere), but not on multiple directions simultaneously. To achieve the best available accuracy with the S_N method, one resorts to Galerkin quadratures that obey certain favorable properties, but these cannot be anisotropically refined either [25]. Finally, standard discrete ordinates codes use source iteration, which tends to break down for increasingly forward-peaked scatter functions. Turcksin et al. [27] devised acceleration methods based on multigrid iteration to address this shortcoming at the price of considerable complexity.

In the present work we investigate a discretization of the Fokker-Planck equation that is based on discontinuous finite elements for the angular discretization. Kópházi and Lathouwers [14] introduced this earlier for neutral particle transport. Here we additionally present the treatment of the Fokker-Planck continuous scatter term through an application of the symmetric interior penalty (SIP) method to the unit sphere. Note that this discretization is also compatible with the use of adaptive mesh refinement [15, 16]. The angular discretization can be refined both *anisotropically* (focusing on certain directions more than others) and *heterogeneously* (with different angular discretizations in various parts of the spatial domain). Neither is addressed by the alternative space-angle DG method proposed recently by Aubin et al. [2]; it's especially unclear how it could support heterogeneous refinement.

This paper is structured as follows. In section 2 we describe the Fokker-Planck equation and its discretization in a single energy group. We pay par-

ticular attention to the formulation of the basis functions, the spherical SIP method, and the spatial streaming term. We briefly describe the solution algorithm used for solving the linear systems. Section 3 illustrates our methodology with three examples of varying complexity, ranging from purely angular dependent to a three-dimensional Fermi pencil-beam case related to radiotherapy applications. Finally, conclusions are drawn and a discussion is given in Section 4.

2 Discretization of the Fokker-Planck transport equation

2.1 The Fokker-Planck equation

In this paper we study the time-independent, mono-energetic Fokker-Planck equation for particle transport, given by

$$\Omega_i \frac{\partial \varphi}{\partial x_i} - \frac{\alpha}{2} \Delta_s \varphi + \Sigma_a \varphi = S, \qquad \mathbf{x} \in E,\ \mathbf{\Omega} \in \mathbb{S}^2 \ , \tag{1}$$

where $\mathbf{x}$ is the position, $\mathbf{\Omega}$ is the unit direction vector, $\varphi = \varphi(\mathbf{x}, \mathbf{\Omega})$ is the angular flux and $S = S(\mathbf{x}, \mathbf{\Omega})$ is an external source. The summation over repeated indices is implied and we use Cartesian coordinates for both $\mathbf{x}$ and $\mathbf{\Omega}$. The spherical Laplacian is $\Delta_s \coloneqq \partial_i^s \partial_i^s$, where ∂^s is the spherical gradient operator with components

$$\partial_i^s = \frac{\partial}{\partial \Omega_i} - \Omega_i \Omega_j \frac{\partial}{\partial \Omega_j} \ . \tag{2}$$

Note that ∂^s acts tangential to the unit sphere, i.e.: $\Omega_i \partial_i^s = 0$. The diffusion constant $\alpha = \alpha(\mathbf{x}) \geq 0$ is called the (macroscopic) transport cross section or momentum transfer, while $\Sigma_a = \Sigma_a(\mathbf{x}) \geq 0$ is the macroscopic absorption cross section.

Equation 1 models cases where the direction vector undergoes a series of small deviations as the particle travels through the medium. The angular diffusion term $(\alpha/2)\Delta_s \varphi$ approximates this random walk of $\mathbf{\Omega}$ over $\mathbb{S}^2$. The model is often used for charged particles, which have a large number of Coulomb interaction with nuclei with small deflections in each collision. The Fokker-Planck approximation is valid in the limit where the angular deflection tends to zero, while the product of angular deflection and collision frequency is kept constant. See [5, 6] for a detailed derivation of equation 1 and an examination of its validity.

Ultimately, the quantity of interest is the scalar flux ϕ, which is the zeroth moment of φ:

$$\phi \coloneqq \langle 1, \varphi \rangle_{\mathbb{S}^2} \ . \tag{3}$$

Here

$$\langle a, b \rangle_H \coloneqq \int_H ab \tag{4}$$

denotes the standard inner product over a domain H. The first moments,

$$j_i \coloneqq \langle \Omega_i, \varphi \rangle_{\mathbb{S}^2} \ , \tag{5}$$

are the components of the angular current density. An important property of the angular diffusion operator $-(1/2)\Delta_s$ is that it preserves particles and the angular current density (see e.g. [22]). Specifically,

$$\langle 1, -(1/2)\Delta_s \varphi \rangle_{\mathbb{S}^2} = 0 \ , \tag{6}$$

$$\langle \Omega_i, -(1/2)\Delta_s \varphi \rangle_{\mathbb{S}^2} = j_i \ . \tag{7}$$

Taking appropriate inner products of equation 1 and using the properties above yields

$$\phi = \frac{1}{\Sigma_a} \left(\langle 1, S \rangle_{\mathbb{S}^2} - \frac{\partial j_i}{\partial x_i} \right) \ , \tag{8}$$

$$j_i = \frac{1}{\Sigma_a + \alpha} \left(\langle \Omega_i, S \rangle_{\mathbb{S}^2} - \frac{\partial}{\partial x_m} \langle \Omega_i \Omega_m, \varphi \rangle_{\mathbb{S}^2} \right) \ . \tag{9}$$

Note that 1 and Ω_i are spherical harmonics of order zero and one respectively. In general, one could consider an arbitrary spherical harmonic Y_{lm} of order l. The corresponding l^{th} moment $\langle Y_{lm}, \varphi \rangle_{\mathbb{S}^2}$ can always be expressed in terms of the spatial derivatives of the $(l+1)^{\text{th}}$ moments.[1] Ideally the conservative properties 6 and 7 also hold discretely.

2.2 Angular diffusion operator

In this section we focus on pure angular dependence, i.e. without spatial streaming. In this case, the transport equation reduces to

$$-\frac{\alpha}{2}\Delta_s u + \Sigma_a u = f(\mathbf{\Omega}) \ , \tag{10}$$

where $u = u(\mathbf{\Omega})$ is the unknown and $\alpha \geq 0$, $\Sigma_a > 0$ are arbitrary constants. The boundary of a sphere is empty, so the absorption term $(\Sigma_a u)$ is necessary to ensure that there is a unique solution for all f. This type of surface partial differential equation occurs in several fields and there are many numerical approaches. Several authors (e.g.: [29, 19]) have suggested finite volume discretizations for the spherical Laplacian. There is also considerable experience with continuous finite elements on general surfaces [11] and unit spheres in particular [17]. Due to their continuous nature, these approaches are incompatible with our treatment of the spatial streaming term. We therefore employ discontinuous basis functions on the sphere, which also simplifies anisotropic refinement. Section 2.2.1 describes how the discrete solution vector is mapped to the solution space. The numerical weak formulation is discussed in section 2.2.2.

2.2.1 The angular solution space

To construct the angular solution space, the sphere is meshed into angular elements. To distinguish from the spatial mesh, we refer to an angular element

[1] To show this explicitly, take an inner product of equation 1 with Y_{lm}. Expand the angular flux into spherical harmonics. Recall that Y_{lm} is an eigenfunction of Δ_s. Finally, note that $\Omega_i Y_{lm}$ is a (linear combination of) spherical harmonic(s) of order $l+1$ [20].

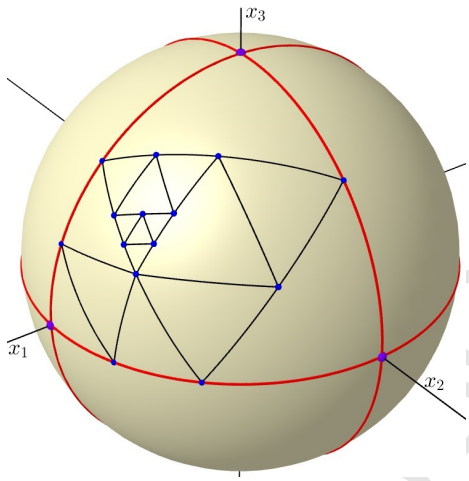

Figure 1: An example of an anisotropically refined spherical mesh.

as a 'patch' and to an angular face as an 'arc'. We choose a simple tessellation with spherical triangles, so that each patch is bounded by three arcs. The initial coarsest mesh consists of the octants of the sphere. Each patch can then be refined by bisecting the great circle segments that make up its boundary, and connecting the midpoints with new great circle segments. Figure 1 displays a possible mesh. A patch is said to be of level l if we need to refine l times to obtain it. In a uniformly refined mesh, the patches asymptotically attain the same shape and size as their level increases [4].

The angular solution space is spanned by a set of basis functions, each of which has support on a single element in the mesh. Let $\Psi_j(\mathbf{\Omega})$ be the basis functions on a patch p. It is convenient to express them as

$$\Psi_i(\mathbf{\Omega}) = C_{ij} b_j(\mathbf{\Omega}) \ , \tag{11}$$

where C is a square nonsingular coefficient matrix. The span is determined by the choice of the functions $b_j(\mathbf{\Omega})$. The coefficients C_{ij} must be chosen such that the local mass matrix

$$M_{ij} \coloneqq \langle \Psi_i, \Psi_j \rangle_p \tag{12}$$

is well-conditioned. This is desirable for DG basis functions in general [24, p. 347-348]. Equations 33 through 35 explicitly show that M should be easy to invert.

There are no non-constant linear functions on $\mathbb{S}^2$, so the choice of basis functions is not obvious. We consider two options:

$\mathbf{\Omega}$-functions are linear in the components of $\mathbf{\Omega}$. That is,

$$\mathbf{b} = \begin{bmatrix} 1 \\ \mathbf{\Omega} \end{bmatrix} \in \mathbb{R}^4 \ . \tag{13}$$

The spherical gradient is

$$\partial_i^s \Psi_j = (\delta_{im} - \Omega_i \Omega_m) \, C_{jn} \frac{\partial}{\partial \Omega_m} b_n \ . \tag{14}$$

Kópházi and Lathouwers [14] showed that $C_{ij} = \delta_{ij}$ leads to problematic rounding errors for the $\mathbf{\Omega}$-functions. Instead, we set C such that

$$\begin{aligned} &\Psi_i(\mathbf{V}^{(j)}) = \delta_{ij}, \quad \Psi_i(\mathbf{\Omega}_T) = 0, \quad \text{for } i = 1,2,3 \ , \\ &\Psi_4(\mathbf{V}^{(j)}) = 0, \quad \Psi_4(\mathbf{\Omega}_T) = 1 \ , \end{aligned} \tag{15}$$

where $\{\mathbf{V}^{(j)}\}_{j=1}^{3}$ are the vertices of p and

$$\mathbf{\Omega}_T \coloneqq \frac{\mathbf{V}^{(1)} + \mathbf{V}^{(2)} + \mathbf{V}^{(3)}}{\left|\left|\mathbf{V}^{(1)} + \mathbf{V}^{(2)} + \mathbf{V}^{(3)}\right|\right|_2} \ . \tag{16}$$

Equations 11 and 13 are substituted into equations 15 to obtain a dense linear system that is solved for C.

octa-functions are linear on the octahedron. They are based on the parametrization in appendix A.1. The basis is linear on a reference triangle $\mathcal{K}^{\text{ref}} \in \mathbb{R}^2$ (equation 48), and mapped to p via an intermediate flat triangle $\mathcal{Z}$ that lies on the octahedron. Specifically, given a $\mathbf{k} \in \mathcal{K}^{\text{ref}}$,

$$\mathbf{b} = \begin{bmatrix} k_1 \\ k_2 \\ 1 - k_1 - k_2 \end{bmatrix} \in \mathbb{R}^3 \ . \tag{17}$$

The spherical gradient is derived in section A.2 and given by equation 61.

We place $\mathcal{Z}$ on the octahedron, as this is the only choice for which the basis on p can be expressed as a linear combination of the bases on the daughters of p, creating a hierarchic structure. This is a desirable property when spatial streaming is introduced in section 2.3. In our experience, setting $C_{ij} = \delta_{ij}$ yields well-conditioned local mass matrices (equation 12) on all patches on all levels of angular refinement.

We note that both types of basis functions can be extended to higher orders in a simple manner, though we did not pursue this possibility here.

2.2.2 A spherical SIP formulation

The combination of a discontinuous angular solution space and a spherical Laplace operator suggests an application of a discontinuous Galerkin interior penalty method to the unit sphere. Fortunately, thoroughly analyzed finite element methods for Euclidean spaces carry over naturally to the spherical domain. This is because integration by parts on a patch p is the same as on a Euclidean element. That is, for sufficiently smooth functions v and w,

$$\langle v, \partial_i^s \partial_i^s w \rangle_p = \langle v, n_{[p]i} \partial_i^s w \rangle_{\partial p} - \langle \partial_i^s v, \partial_i^s w \rangle_p \ , \tag{18}$$

where the outward unit normal $\mathbf{n}_{[p]}$ is tangential to the sphere [11].

Take an inner product of equation 10 with a test function v and integrate by parts to find the discrete weak form

Find $u_\ell \in S_\ell$, such that, for all $v \in S_\ell$,

$$\frac{\alpha}{2}\left(\sum_{p\in\mathcal{P}_\ell} \langle \partial_i^s u_\ell, \partial_i^s v \rangle_p + \sum_{a\in\mathcal{A}_\ell} b_{[a]}(u_\ell, v)\right) + \Sigma_a \langle u_\ell, v \rangle_{\mathbb{S}^2} = \langle f, v \rangle_{\mathbb{S}^2} \ , \tag{19}$$

where S_ℓ is the angular solution space, $\mathcal{P}_\ell$ is the angular mesh with characteristic length scale ℓ, and $\mathcal{A}_\ell$ is the set of arcs in $\mathcal{P}_\ell$. We consider only the symmetric interior penalty (SIP) method [24, 8], where the bilinear operator $b_{[a]} : v, w \in (S_\ell \times S_\ell) \to \mathbb{R}$ is defined as follows. For all $a \in \mathcal{A}_\ell$, define a characteristic length scale ℓ_a and choose an arbitrary but fixed ordering of its neighboring patches p_1 and p_2. Denote by $\mathbf{n}_{[a]}$ the normal vector that points from p_1 to p_2. Define the jump and averaging operators by

$$[\![\cdot]\!]_a \coloneqq \cdot|_{p_1} - \cdot|_{p_2} \qquad \text{and} \qquad \{\cdot\}_a \coloneqq \frac{1}{2}\left(\cdot|_{p_1} + \cdot|_{p_2}\right) \tag{20}$$

respectively. On vectors they act component-wise. Now

$$\begin{aligned} b_{[a]}(v, w) \coloneqq &- \left\langle [\![w]\!]_a, n_{[a]i} \left\{\partial_i^s v\right\}_a \right\rangle_a - \left\langle [\![v]\!]_a, n_{[a]i} \left\{\partial_i^s w\right\}_a \right\rangle_a \\ &+ \frac{\eta}{\ell_a} \left\langle [\![v]\!]_a, [\![w]\!]_a \right\rangle_a \ , \end{aligned} \tag{21}$$

where η is the penalty parameter.

The penalty parameter should be large enough to ensure coercivity of the bilinear form, but high values degrade the quality of the solution and increase the condition number of the linear system [24]. We follow Shahbazi [26] and Epshteyn and Rivière [12], who recommend $\eta = 3$ for linear basis functions on meshes with equilateral triangles. Note that our patches asymptotically become flat as the angular refinement increases. We set ℓ_a equal to the length of a. We have successfully tested the SIP method with these parameters extensively on various angular meshes, including randomly refined meshes where adjacent patches can have a difference in angular refinement of up to 4 levels.

There are myriad other DG discretizations of the poisson equation, including the local DG (LDG) method [7], various interior penalty (IP) methods [1] and the cell-centered Galerkin (ccG) method [9]. The advantages of SIP method include its compact stencil and optimal convergence rate for all orders of basis functions. The adjoint consistency of the SIP method enables adaptive mesh refinement in future work.

An attractive property of the discretization is that it is locally conservative, as can be seen by substituting one of the basis functions for v in equation 19 [24, p. 142]. This means that the numerical scheme satisfies the property in equation 6 if the solution space contains a constant function, which is always the case. Equation 7 also holds discretely if $\mathbf{\Omega}$ lies in the solution space, which is true for every angular mesh with $\mathbf{\Omega}$-functions.

2.3 Spatial streaming

This section describes the DG method for the full space-angle problem given by equation 1 on a spatial domain E with two types of boundary conditions:

$$\text{Dirichlet:} \qquad \varphi(\mathbf{x}, \mathbf{\Omega}) = \varphi^{\mathrm{D}}(\mathbf{x}, \mathbf{\Omega}) \qquad \text{for } \mathbf{\Omega} \cdot \mathbf{n}_E < 0 \ , \tag{22}$$

$$\text{reflective:} \qquad \varphi(\mathbf{x}, \mathbf{\Omega}) = \varphi\left(\mathbf{x}, \mathbf{\Omega}^{\mathrm{refl}}\right) \qquad \text{for } \mathbf{\Omega} \cdot \mathbf{n}_E < 0 \ , \tag{23}$$

where $\mathbf{n}_E$ is the outward normal of E and $\mathbf{\Omega}^{\mathrm{refl}} \coloneqq \mathbf{\Omega} - 2(\mathbf{\Omega} \cdot \mathbf{n}_E)\mathbf{n}_E$ is the reflection of $\mathbf{\Omega}$ in the boundary.

The solution space is constructed as follows. Let $\mathcal{T}_h$ be the spatial mesh with characteristic length h. The set of faces that border an element $j \in \mathcal{T}_h$ is $\mathcal{F}_{[j]}$. Denote by $\mathbf{n}_{[f]}$ the normal of face f, pointing in an arbitrary but fixed direction. For simplicity, every face is assumed flat: its normal is constant. On each element j we define spatial basis functions $\Phi_{[j]l} = \Phi_{[j]l}(\mathbf{x})$, which span all polynomials up to order p with support on j. Each element j is equipped with an angular mesh $\mathcal{P}(j)$. On each patch $q \in \mathcal{P}(j)$, we define the angular basis functions $\Psi_{[q]m} = \Psi_{[q]m}(\mathbf{\Omega})$, as explained in section 2.2.1. We use the same type of angular basis functions on all patches in all angular meshes. The set of arcs that border patch q is $\mathcal{A}_{[q]}$. Within an element k and patch p, the solution space is spanned by the products of spatial and angular basis functions. In other words, the numerical solution is of the form

$$\varphi_h(\mathbf{x}, \mathbf{\Omega}) = \sum_{k \in \mathcal{T}_h} \Phi_{[k]i}(\mathbf{x}) \sum_{p \in \mathcal{P}(k)} \Psi_{[p]d}(\mathbf{\Omega})\, c_{[k,p]id} \tag{24}$$

where $c_{[k,p]id}$ are the solution coefficients on a patch p in the angular mesh of element k. We emphasize that each element can have its own angular mesh, and all elements and patches can be refined locally.

To derive a weak form, we take an inner product of equation 1 with a basis function $\Phi_{[j]l}(\mathbf{x})\Psi_{[q]m}(\mathbf{\Omega})$. Substituting the continuous product solution $\varphi(\mathbf{x}, \mathbf{\Omega}) = R(\mathbf{x})Q(\mathbf{\Omega})$, the angular diffusion term becomes

$$\begin{aligned}
&\left\langle -\frac{\alpha}{2}\Delta_s RQ,\ \Phi_{[j]l}\Psi_{[q]m} \right\rangle_{E\times\mathbb{S}^2} \\
&= \left\langle \frac{\alpha}{2}R,\ \Phi_{[j]l} \right\rangle_j \left\langle -\Delta_s Q,\ \Psi_{[q]m} \right\rangle_q \\
&= \left\langle \frac{\alpha}{2}R,\ \Phi_{[j]l} \right\rangle_j \left(\left\langle \partial_\xi^s Q,\ \partial_\xi^s \Psi_{[q]m} \right\rangle_q - \sum_{a \in \mathcal{A}_{[q]}} \left\langle n_{[q]\xi}\partial_\xi^s Q,\ \Psi_{[q]m} \right\rangle_a \right) ,
\end{aligned} \tag{25}$$

where we integrated by parts in $\mathbf{\Omega}$ in the last equality. To derive a discrete weak form we substitute $\varphi = \varphi_h$. On an element j this means $R(\mathbf{x})Q(\mathbf{\Omega}) = \Phi_{[j]i}\chi_{[j]i}$, where

$$\chi_{[j]i} = \chi_{[j]i}(\mathbf{\Omega}) = \sum_{p \in \mathcal{P}(j)} \Psi_{[p]d}(\mathbf{\Omega})\, c_{[j,p]id} \tag{26}$$

is the angular flux on element j that corresponds to the spatial basis function $\Phi_{[j]i}(\mathbf{x})$ (compare to equation 24). We replace the boundary term in equation 25 with the SIP boundary operator given by equation 21, ending up with the term

$$\left\langle \frac{\alpha}{2}\Phi_{[j]i}, \Phi_{[j]l} \right\rangle_j \left(\left\langle \partial_\xi^s \Psi_{[q]d}, \partial_\xi^s \Psi_{[q]m} \right\rangle_q c_{[j,q]id} + \sum_{a \in \mathcal{A}_{[q]}} b_{[a]} \left(\chi_{[j]i},\ \Psi_{[q]m} \right) \right) .$$

We proceed in a similar manner for the spatial streaming term in equation 1,

integrating by parts in $\mathbf{x}$ (see also [14]). The result is

$$\begin{aligned}
&-\left\langle \Phi_{[j]i}, \frac{\partial}{\partial x_\xi}\Phi_{[j]l} \right\rangle_j \left\langle \Omega_\xi \Psi_{[q]d}, \Psi_{[q]m} \right\rangle_q c_{[j,q]id} + \sum_{f\in\mathcal{F}_{[j]}} \Upsilon_{[f,j,q]lm} \\
&+\left\langle \frac{\alpha}{2}\Phi_{[j]i}, \Phi_{[j]l} \right\rangle_j \left(\left\langle \partial_\xi^s \Psi_{[q]d}, \partial_\xi^s \Psi_{[q]m} \right\rangle_p c_{[j,q]id} + \sum_{a\in\mathcal{A}_{[q]}} b_{[a]} \left(\chi_{[j]i},\ \Psi_{[q]m}\right) \right) \\
&+\left\langle \Sigma_a \Phi_{[j]i}, \Phi_{[j]l} \right\rangle_j \left\langle \Psi_{[q]d}, \Psi_{[q]m} \right\rangle_q c_{[j,q]id} \\
=\quad &\left\langle S, \Phi_{[j]l}\Psi_{[q]m} \right\rangle_{j\times q} \ .
\end{aligned} \tag{27}$$

The boundary term $\Upsilon_{[f,j,q]}$ arose from integrating by parts in $\mathbf{x}$ and still needs to be discretized. It represents the effect of spatial streaming though a face f on patch $q \in \mathcal{P}(j)$. It couples the patch q with all overlapping patches in the angular mesh of the neighbor of j at face f. It therefore has the form

$$\begin{aligned}
\Upsilon_{[f,j,q]lm} = \sum_{q'\in\wedge\left(q,\mathcal{P}(j'_f)\right)} \Big(\quad & S^-_{[f,j]li} F^-_{[f,q,q']md}\ c_{[j'_f,q']id} \\
& + S^+_{[f,j]li} F^+_{[f,q,q']md}\ c_{[j,q]id} \Big) \ ,
\end{aligned} \tag{28}$$

where

$$S^-_{[f,j]li} \coloneqq \left\langle \Psi_{[j]l}, \Psi_{[j'_f]i} \right\rangle_f \ , \tag{29}$$

$$S^+_{[f,j]li} \coloneqq \left\langle \Psi_{[j]l}, \Psi_{[j]i} \right\rangle_f \ , \tag{30}$$

j'_f is the neighbor of j at face f, and $\wedge\left(q,\mathcal{P}(j'_f)\right)$ is the set of all patches in $\mathcal{P}(j'_f)$ that overlap with q. From the perspective of q, the terms involving $F^-_{[f,q,q']}$ and $F^+_{[f,q,q']}$ respectively represent inflow and outflow across face f.

We define $F^\pm_{[f,q,q']}$ in accordance with the conservative upwinded numerical flux suggested by Kópházi and Lathouwers [14]. The term

$$A_{[f,q]md} \coloneqq \left\langle \mathbf{n}_{[f]} \cdot \mathbf{\Omega}\ \Psi_{[q]d}, \Psi_{[q]m} \right\rangle_q \ . \tag{31}$$

arises naturally from the partial integration that led to equation 27. For example, if there is only inflow (so $F^+_{[f,q,q']} = 0$), and the patches q and q' have the same level, then $F^-_{[f,q,q']} = A_{[f,q]md}$. To separate inflow and outflow in the general case, we perform an eigenvalue decomposition of $A_{[f,q]}$ where

$$M_{[q,p]md} \coloneqq \left\langle \Psi_{[q]m}, \Psi_{[p]d} \right\rangle_q \tag{32}$$

is the metric. That is, we determine the unique matrix $P_{[f,q]}$ such that

$$A_{[f,q]} = M_{[q,q]} \left(PGP^{-1}\right)_{[f,q]} \ , \tag{33}$$

where $G_{[f,q]}$ is a diagonal matrix. Let

$$A^\pm_{[f,q]} \coloneqq M_{[q,q]} \left(PG^\pm P^{-1}\right)_{[f,q]} \ , \tag{34}$$

where G^- (resp. G^+) is constructed by replacing the positive (resp. negative) values in G with zeros, so that $G = G^- + G^+$ and $A = A^- + A^+$. We also introduce

$$L_{[q,q']} \coloneqq M_{[q,q']} M^{-1}_{[q',q']} \qquad \text{and} \qquad H_{[q,q']} \coloneqq M^{-1}_{[q,q]} M_{[q,q']} \ . \tag{35}$$

These operators are Galerkin projections, with $L_{[q,q']}$ mapping from a coarse patch q to a finer patch q', and $H_{[q,q']}$ mapping from a fine patch q to a coarser patch q'. Note that the Galerkin projections are exact if the basis on a patch can be expressed as a linear combination of the bases on its daughters. For the definition of $F^{\pm}_{[f,q,q']}$, Kópházi and Lathouwers [14] considered separate cases, depending on the difference in the levels of angular refinement of the patches q and q'. The results can be summarized in an insightful way by rewriting equation 28 as

$$\begin{aligned} \Upsilon_{[f,j,q]lm} = \sum_{q' \in \wedge\left(q, \mathcal{P}(j'_f)\right)} \Bigg(& S^-_{[f,j]li} \left(L_{[q,s]} A^-_{[f,s]} H_{[s,q']} \right)_{md} c_{[j'_f,q']id} \\ & + S^+_{[f,j]li} \left(L_{[q,s]} A^+_{[f,s]} H_{[s,q]} \right)_{md} c_{[j,q]id} \Bigg)_{s=\min(q,q')} \ . \end{aligned} \tag{36}$$

Here $s = \min(q, q')$ is the smaller of the two patches (that is, the one with the highest level of angular refinement). The first term in the products ($S^{\pm}_{[f,j]}$) is the usual finite element term that arises from an integration of the governing equation. The term $L_{[q,s]}$ translates the result from the angular basis on q to the angular basis on s, the smallest of the patches, where $A^{\pm}_{[f,s]}$ separates the incoming and outgoing flux. Finally, $H_{[s,q']}$ maps back from s to q'. If the patch q is larger than the patches from/to which the flux streams, then the upwinding scheme is performed by summing over the contributions in smaller patches in $\wedge\left(q, \mathcal{P}(j'_f)\right)$. This ensures a symmetry in the upwinding scheme between two patches that are not of equal size, making the numerical method conservative.

The generalized eigenvalue decomposition in equation 33 can be avoided if $\mathbf{n}_{[f]} \cdot \mathbf{\Omega}$ has a constant sign for all $\mathbf{\Omega} \in q$, because then either $G^-_{[f,q]} = 0$ or $G^+_{[f,q]} = 0$. Specifically,

$$F^-_{[f,q,q']} = L_{[q,s]} A_{[f,s]} H_{[s,q']} \ , \quad F^+_{[f,q,q']} = 0 \ , \quad \text{if } \mathbf{\Omega} \cdot \mathbf{n}_{[f]} < 0 \text{ for all } \mathbf{\Omega} \in q, \tag{37}$$

$$F^+_{[f,q,q']} = L_{[q,s]} A_{[f,s]} H_{[s,q]} \ , \quad F^-_{[f,q,q']} = 0 \ , \quad \text{if } \mathbf{\Omega} \cdot \mathbf{n}_{[f]} > 0 \text{ for all } \mathbf{\Omega} \in q, \tag{38}$$

where $s = \min(q, q')$. Physically, these are cases where there is either no inflow or no outflow through q. As the angular meshes are refined, the patches become flatter, and the percentage of patches that require an explicit eigenvalue decomposition drops sharply.

A practical implementation of the weak form (equation 27) is facilitated by the fact that the spatial and angular integrals are split. If we store them as matrices, then all contributions to the global linear system are Kronecker products of the spatial and angular integral matrices. The required memory is limited by storing the angular integrals on a 'master sphere', which is an angular discretization that contains all patches in all angular meshes.

2.4 Solution Strategy

In discrete ordinates discretizations of the Boltzmann equation, one traditionally uses source iteration to converge the equations. In this method, the scatter source is based on the currently known solution and thereafter the angular solution is updated by performing a transport sweep where the equations are inverted with the scatter source fixed. This procedure is effective when the scatter-ratio is not too large. For highly diffusive media, there are acceleration methods such as DSA, leading to unconditionally effective schemes when combined with Krylov subspace methods [28].

In the present angular discretization that is based on finite element basis functions on the sphere, the Riemann procedure is used to determine the directionality of information crossing the element faces. The elements can be mutually dependent, so there is no straightforward ordering of spatial elements that makes the linear system (block) triangular. In previous work [14] we devised a solution strategy that is based on an approximate sweep that was found to be effective in the test problems. The method constructs sweep orderings that correspond to an S_2 direction set. Each direction is associated with an octant of the sphere and the patches it contains. For each direction, the spatial elements are visited in the prescribed order. On each spatial element, the angular patches corresponding to the direction (octant) are sequentially visited and the local linear systems are solved for. This sweep-based method is compatible with the discretization where patches are locally decoupled from other patches due to the use of discontinuous angular basis functions, contrary to other methods such as spherical harmonics and wavelets. To a large extent this approach retains the high efficiency associated with sweep algorithms to our angular finite element discretization. Details can be found in [14]. The sweep-based algorithm is used as a preconditioner to a Krylov subspace method (BiCGSTAB) to construct a robust method. We iterate until the L_2-norm of the residual of the linear system is at most 10^{-12} times the L_2-norm of the right hand side.

In the present work, the spherical diffusion operator is added to the equation, which adds coupling between patches. For increasing values of the transport cross section, α, this deteriorates the efficiency of the algorithm. Improving the efficiency by using a more suitable preconditioner that captures the diffusive coupling between patches is likely to perform better. Here, we concentrate on the discretization and postpone solver improvements to future work.

3 Numerical examples

To illustrate our Fokker-Planck discretization technique, we have applied the method to three problems: (i) a purely angular manufactured solution without spatial streaming, (ii) a manufactured solution that depends on both space and angle and (iii) a three-dimensional Fermi pencil beam problem.

Table 1: Results of the spherical SIP method on uniformly refined meshes $\mathcal{P}_\ell$ with the exact solution 39. The error e_ℓ is given by equation 40. The order of convergence on $\mathcal{P}_\ell$ is estimated with a comparison with the result on $\mathcal{P}_{2\ell}$. The last column lists the order of convergence of a component of the current.

	$\mathbf{\Omega}$-*functions*		*octa-functions*		
$\mathrm{card}(\mathcal{P}_\ell)$	e_ℓ	order of e_ℓ	e_ℓ	order of e_ℓ	order of $\lvert\langle\Omega_3, u_\ell\rangle_{\mathbb{S}^2} - j_3\rvert$
$8 \cdot 4^0$	$2.288e{-1}$	-	$2.462e{-1}$	-	-
$8 \cdot 4^1$	$8.853e{-2}$	1.37	$1.271e{-1}$	0.95	5.60
$8 \cdot 4^2$	$2.268e{-2}$	1.96	$3.528e{-2}$	1.85	1.40
$8 \cdot 4^3$	$5.802e{-3}$	1.97	$9.100e{-3}$	1.95	1.71
$8 \cdot 4^4$	$1.455e{-3}$	2.00	$2.305e{-3}$	1.98	1.98
$8 \cdot 4^5$	$3.611e{-4}$	2.01	$5.818e{-4}$	1.99	2.00

3.1 A purely angular problem

We used the method outlined in section 2.2 to obtain a numerical solution for equation 10, where the source term f was set such that the exact solution is

$$\begin{aligned} u &= Y_{00} - Y_{21} + Y_{30} \\ &= \frac{1}{\sqrt{4\pi}} \left(1 - 15\Omega_1\Omega_2 + \frac{1}{2}\sqrt{7}\left(\Omega_1\left(2{\Omega_1}^2 - 3\Omega_2 - 3{\Omega_3}^2\right)\right)\right) , \end{aligned} \tag{39}$$

where $Y_{lm}(\mathbf{\Omega})$ are the normalized real spherical harmonics, i.e.: $\langle Y_{lm}, Y_{l'm'}\rangle_{\mathbb{S}^2} = \delta_{ll'}\delta_{mm'}$. We set $\Sigma_a = 1/10$ and $\alpha = 1/4$. We used a direct solver for the linear system. The relative global L_2-error on a mesh S_ℓ is defined by

$$e_\ell \coloneqq \frac{|u_\ell - u|_{\mathbb{S}^2}}{|u|_{\mathbb{S}^2}} , \tag{40}$$

Here $|\cdot|_H$ denotes the norm on a domain H that corresponds to the inner product in equation 4. Table 1 lists the errors for both types of basis functions. We observe the expected second order convergence for both basis function sets. The two types of basis functions have an approximately equal error per degree of freedom, with the $\mathbf{\Omega}$-functions being slightly more efficient. The numerical angular current density (equation 5) is exact for the $\mathbf{\Omega}$-functions and therefore not listed. For the octa-functions it converges quadratically. In general, the convergence is slower on coarse meshes for two reasons. First, the solution is insufficiently smooth within the patches. Second, the basis functions are approximately linear only on small patches. The octa-functions in particular can have highly irregular shapes on large patches.

We performed several more tests with different positive values for α and Σ_a and various manufactured solutions. The results were similar to those in table 1.

3.2 A two-dimensional problem

To study the convergence of the numerical scheme with spatial streaming from section 2.3, we performed a series of simulations where the exact solution is

Table 2: Orders of convergence for the 2D problem of section 3.2 on the finest spatial mesh ($h = 0.0038$) as the angular mesh is refined. The order for an angular mesh $\mathcal{P}_\ell$ is estimated with a comparison with the error on $\mathcal{P}_{2\ell}$.

	$\boldsymbol{\Omega}$-*functions*		*octa-functions*	
$\mathrm{card}(\mathcal{P}_\ell)$	order of $e^{\mathrm{ang}}_{h,\ell}$	order of $e^{\mathrm{scal}}_{h,\ell}$	order of $e^{\mathrm{ang}}_{h,\ell}$	order of $e^{\mathrm{scal}}_{h,\ell}$
$8 \cdot 4^1$	1.34	2.56	0.91	2.32
$8 \cdot 4^2$	1.97	2.50	1.86	2.12
$8 \cdot 4^3$	1.96	1.15	1.95	1.90

known. We set $\Sigma_a = 10$, $\alpha = 1$ and set the source and the boundary conditions such that the solution is quadratic in both space and angle:

$$\varphi(\mathbf{x}, \boldsymbol{\Omega}) = x_1(1 - x_1)x_2(1 - x_2)\left(4 + \Omega_1 + 2\Omega_2 + 3{\Omega_1}^2\right) \ . \tag{41}$$

The spatial domain is $E = (0, 1)^2$. The spatial mesh is unstructured and consists of triangles of approximately equal size and shape with basis functions of order $p = 1$. We define the characteristic mesh length as $h = \mathrm{card}(\mathcal{T}_h)^{-1/2}$. We use the same homogeneously refined angular mesh for all elements and vary the level of angular refinement. For an angular mesh $\mathcal{P}_\ell$, the relative L_2-error of the angular flux is

$$e^{\mathrm{ang}}_{h,\ell} \coloneqq \frac{|\varphi_h - \varphi|_{T\times\mathbb{S}^2}}{|\varphi|_{T\times\mathbb{S}^2}} \tag{42}$$

and the relative L_2-error of the scalar flux is

$$e^{\mathrm{scal}}_{h,\ell} \coloneqq \frac{|\phi_h - \phi|_T}{|\phi|_T} \ . \tag{43}$$

We use the solution method described in section 2.3.

Figure 2 shows the relative L_2-errors of the angular flux and the scalar flux for various angular refinement levels l. The orders of convergence on the finest spatial mesh are tabulated in table 2. We observe the same second order convergence in the angular discretization as in the previous test case. The convergence clearly saturates at high angular refinements, where the spatial discretization affects the errors significantly. The errors are roughly an order of magnitude lower for the scalar flux than for the angular flux, and consequently saturation occurs much sooner for the scalar flux. The order of convergence between levels 0 and 1 in figure 2a indicates that the angular flux is poorly resolved on these angular meshes. Nevertheless, the scalar flux (figure 2b) does show immediate second order convergence as the level increases from 0. Interestingly, the scalar flux initially converges faster than with second order, especially for the $\boldsymbol{\Omega}$-functions.

3.3 Three-dimensional Fermi pencil beam

Our final problem is a three-dimensional Fermi pencil-beam calculation. In radiotherapy applications, physical pencil beams are used to deliver the radiation.

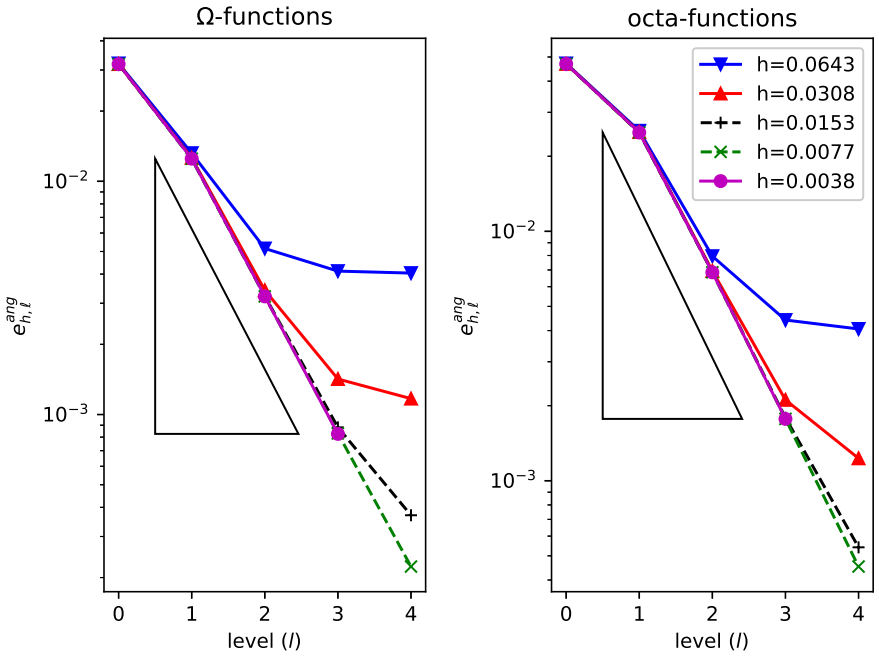

(a) relative L_2-error of angular flux (equation 42)

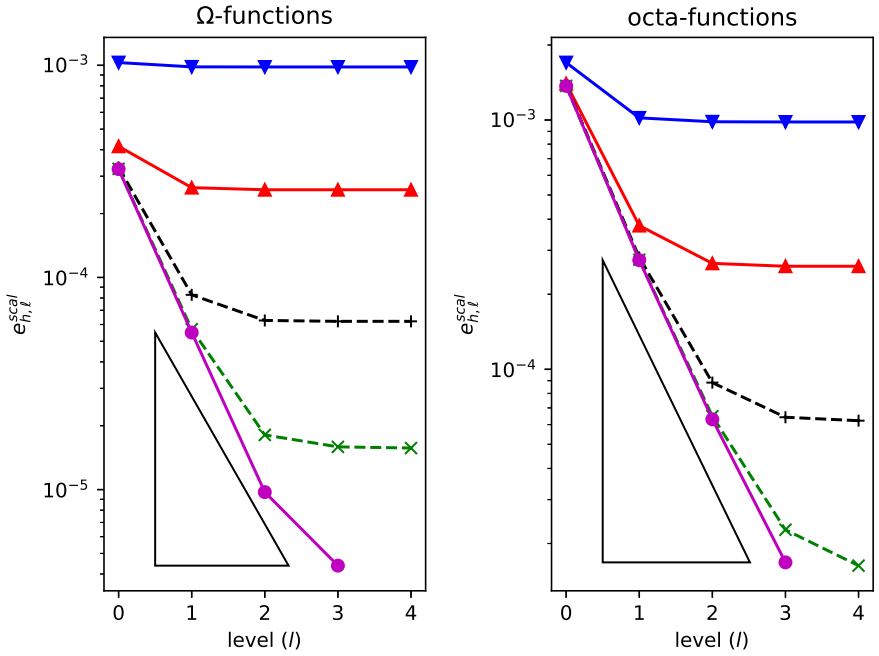

(b) relative L_2-error of scalar flux (equation 43)

Figure 2: Convergence to exact solution (equation 41) as the angular mesh is refined on various spatial meshes with characteristic length h. The triangles indicate ideal second order convergence in the angular discretization.

A frequently used model for treatment planning (optimization) is the use of the Fermi pencil-beam model which is an approximation to the Fokker-Planck model. The mathematical problem is as follows: Consider the half-infinite domain $x_1 > 0$, with

$$\varphi = \delta(x_2)\delta(x_3)\frac{\delta(1-\Omega_1)}{2\pi} \ , \qquad \text{for } x_1 = 0 \text{ and } \Omega_1 > 0 \ , \tag{44}$$

where $\delta(\cdot)$ is the Dirac delta function. In the absence of absorption (i.e.: $\Sigma_a = 0$), the Fermi pencil beam approximation is

$$\varphi \approx \varphi^{\mathrm{F}} = \frac{3}{\pi^2\alpha^2{x_1}^4}\exp\left(-\frac{2}{\alpha}\left(\frac{{\Omega_2}^2+{\Omega_3}^2}{x_1} - 3\frac{\Omega_2 x_2 + \Omega_3 x_3}{{x_1}^2} + 3\frac{{x_2}^2+{x_3}^2}{{x_1}^3}\right)\right) \ . \tag{45}$$

This approximation is derived under the assumption of small-angle scattering. Since φ is small everywhere except when ${\Omega_2}^2 + {\Omega_3}^2 \ll 1$, an approximate scalar flux can be found by extending the range of integration to $\Omega_2, \Omega_3 \in \mathbb{R}$, yielding

$$\phi^{\mathrm{F}} \approx \int_{\mathbb{R}^2} \varphi^{\mathrm{F}} \ \mathrm{d}(\Omega_2, \Omega_3) = \frac{3}{2\pi\alpha{x_1}^3}\exp\left(-\frac{3}{2\alpha}\ \frac{{x_2}^2+{x_3}^2}{{x_1}^3}\right) \ . \tag{46}$$

The reader is refered to Börgers and Larsen [5] for a more in-depth discussion of the pencil-beam model and the Fermi approximation.

In practical applications, the physical pencil beam has a finite width at the entrance, which can be modeled as a set of mathematical pencil beams with varying weights. To avoid the singularity of the pencil-beam model in our calculation, we exclude points close to $x_1 = 0$ and limit the computational domain to

$$3/10 < x_1 < 1; \quad 0 < x_2, x_3 < 2/5 \ . \tag{47}$$

We employ Dirichlet boundary conditions $\varphi^{\mathrm{D}} = \varphi^{\mathrm{F}}$ on $x_1 = 3/10$, reflective conditions on $x_2 = 0$ and $x_3 = 0$ and vacuum conditions on all other boundary faces. We set $\Sigma_a = 0$ and $\alpha = 1/10$.

Figure 3 shows the numerical scalar flux in the domain. The unstructured tetrahedral mesh was generated by the `Gmsh` software library [13]. The highest resolution is located near the central axis of the beam and near the inlet region. The angular mesh is shown in figure 4; it is the same for all spatial elements. It is refined near the Ω_1-pole to capture the forward nature of the radiation problem.

Figure 5 shows the numerical scalar flux along the axis $x_2 = x_3 = 0$. It is clearly in agreement with the Fermi prediction, verifying the ability of the numerical scheme to capture forward-peaked solutions and scatter. The error is highest near the inlet boundary ($x_1 = 3/10$), suggesting that the error is due to the spatial mesh. Our mesh refinement studies confirm this: increasing the angular refinement did not significantly impact the numerical solution.

Although the Fermi approximation is highly accurate near the axis, it incorrectly predicts that the integral of the scalar flux over the lateral plane is constant. Specifically, the approximation in equation 46 implies $\int_{\mathbb{R}^2} \phi^{\mathrm{F}} \ \mathrm{d}(x_2, x_3) = 1$, which we would not have found, had we integrated the angular flux in equation 45 exactly. Figure 6 shows the lateral integrals as a function of penetration depth. Unlike the Fermi prediction, the lateral integrals for the numerical scalar flux increase with x_1 due to a nonzero scattering angle, as expected.

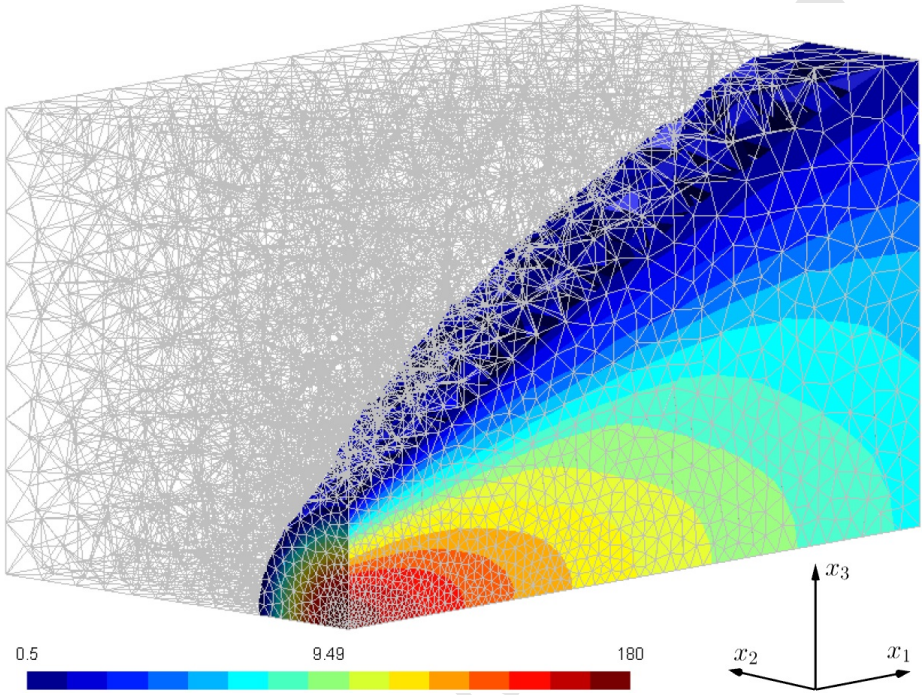

Figure 3: Numerical scalar flux for the Fermi case of section 3.3. The spatial mesh has 17,530 elements. Note the logarithmic scaling in the color map. Small values are left out. There were negative values far from the axis.

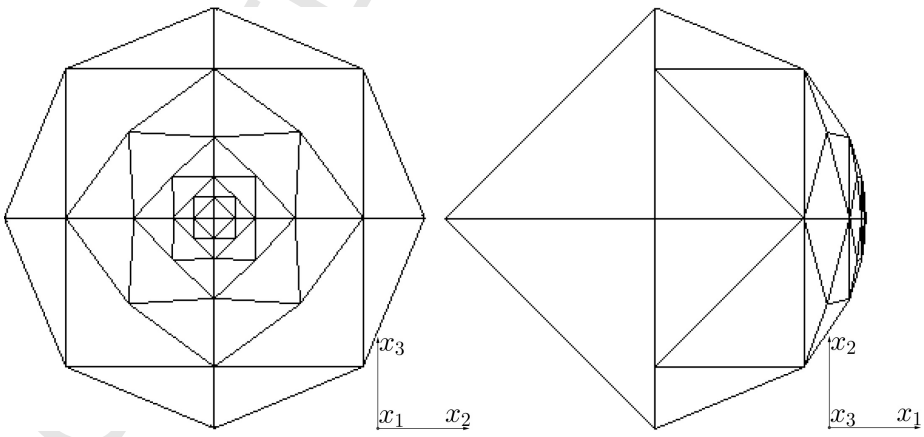

Figure 4: Angular mesh for the Fermi case of section 3.3. It has 56 elements. In this image the arcs are drawn as straight lines instead of great circle segments.

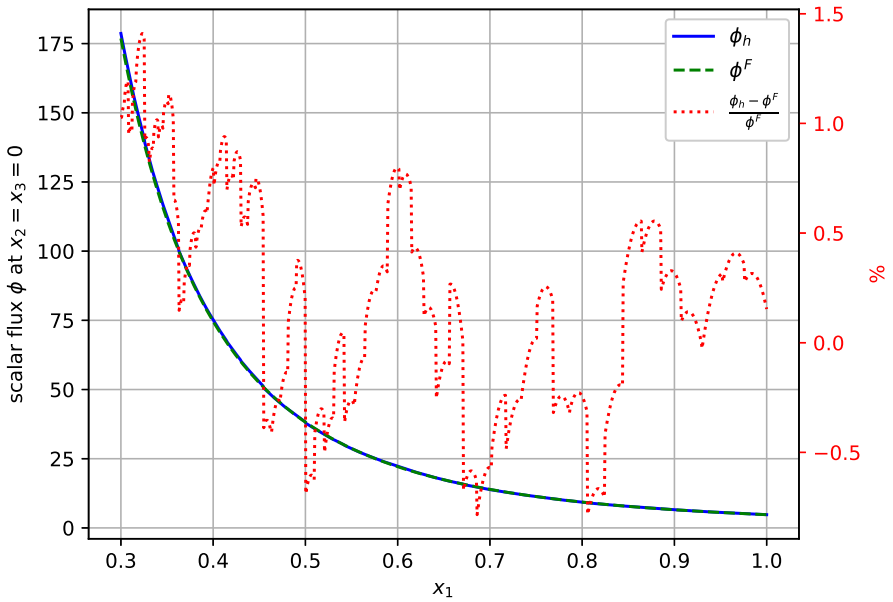

Figure 5: Comparison of Fermi prediction (ϕ^{F}) and numerical value (ϕ_h) of the scalar flux along the axis $x_2 = x_3 = 0$ for the case of section 3.3.

4 Conclusions and Discussion

We have presented a new method for the discretization of the Fokker-Planck equation using discontinuous finite elements in both space and angle. The novelty of the method lies in the use of the symmetric interior penalty method on the spherical surface. With this choice we are able to refine the angular mesh both anisotropically and heterogeneously with a hierarchical set of angular elements, focusing on the points in phase-space that matter most. This contrasts with the standard discrete ordinates method, which cannot be refined hierarchically or anisotropically. Even a product quadrature set, which can focus on a particular pole in the problem, does not have the flexibility of the present scheme. Our method shows promise for radiotherapy applications where multiple beam angles are used and need to be resolved. In this way we expect to obtain (near) Monte-Carlo quality dose distributions at reduced cost and without statistical uncertainty.

In the present work we focus on the discretization method and the rate of convergence of the obtained solution. We used two types of angular basis functions, octa-functions and $\mathbf{\Omega}$-functions, both of which conserve particles exactly. The example problems show the discretization to be second order accurate in angle, which is sufficient for practical application. The results in section 3.2 show that the order of convergence for the scalar flux is greater than 2, even when the angular flux is not yet converged. The scalar flux seems to converge particularly fast for the $\mathbf{\Omega}$-functions, probably because they preserve the angular current density exactly, unlike the octa-functions.

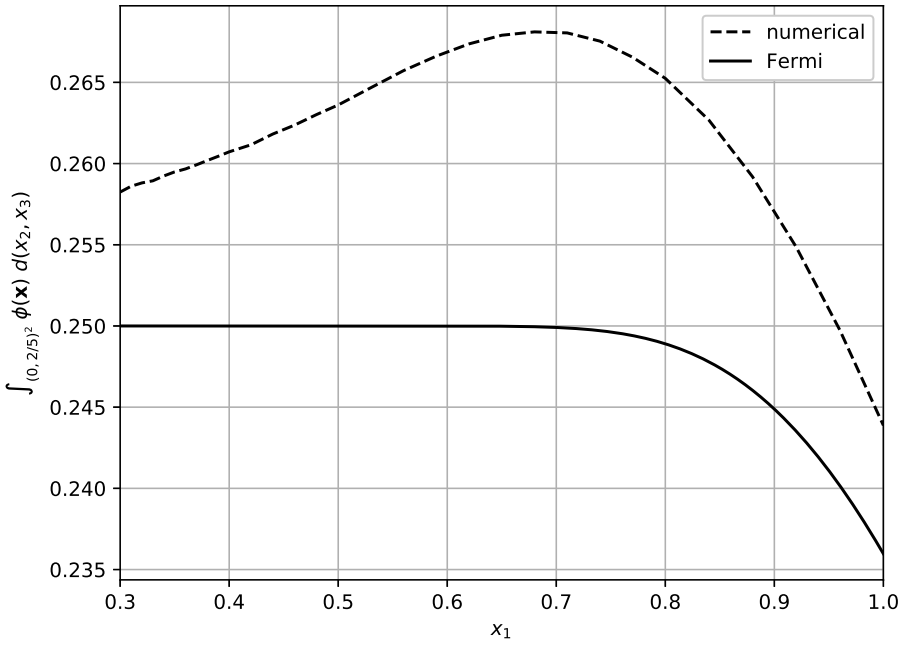

Figure 6: Integrals of the scalar flux over lateral planes in the domain for the Fermi case of section 3.3. Due to the limited size of our domain, the values drop at large penetration depths, where the scalar flux at the boundaries $x_2 = 2/5$ and $x_3 = 2/5$ is no longer negligible.

We plan to address the solution algorithm in future work. Source-iteration is known to be ineffective for the type of forward-peaked scatter that we study [27]. Therefore our solution methodology is not the most effective when the momentum transfer is strong. In the cases where it is, the Fokker-Planck equation is dominated by the spherical Laplacian and the efficacy of the sweep-based algorithm decreases. A multigrid method in angle should be effective for the angular diffusion. Such a solution method is perfectly in line with our hierarchical tessellation of the sphere.

We will also investigate automated spatial and angular refinement and the use of higher order angular functions. Other future work will focus on topics that are of interest for real-life radiotherapy applications. This includes an efficient energy discretization. Also, it's not easy to deal with Dirichlet boundary conditions for highly peaked external beams. It would be better to use a first collision source algorithm. Finally, we expect the same numerical scheme to be effective for more general forward-peaked scatter kernels for charged particles, not just the Fokker-Planck approximation.

A Details of octa-functions

A.1 Parameterization of a spherical triangle

This section details a family of bijections between a reference element

$$\mathcal{K}^{\text{ref}} \coloneqq \{\mathbf{k} \in \mathbb{R}^2 : k_1 > 0, k_2 > 0, k_1 + k_2 < 1\} \tag{48}$$

and an arbitrary spherical triangle $\mathcal{V}$ with vertices $\{\mathbf{V}^{(p)}\}_{p=1}^3$, defined as the open set of all $\mathbf{\Omega} \in \mathbb{S}^2$ that satisfy

$$\text{sign}\left(\mathbf{V}^{(m)} \cdot \left(\mathbf{V}^{(n)} \times \mathbf{V}^{(k)}\right)\right) = \text{sign}\left(\mathbf{\Omega} \cdot \left(\mathbf{V}^{(n)} \times \mathbf{V}^{(k)}\right)\right) \neq 0 \tag{49}$$

for all permutations of $\{m, n, k\}$. Note that this definition excludes singular spherical triangles: the vertices $\{\mathbf{V}^{(p)}\}_{p=1}^3$ must not lie on a single great circle. In words, $\mathcal{V}$ is the smallest subset of $\mathbb{S}^2$ whose boundary consists of the three great circle segments that intersect $\mathbf{V}^{(1)}$, $\mathbf{V}^{(2)}$ and $\mathbf{V}^{(3)}$. The bijection $\mathcal{K}^{\text{ref}} \leftrightarrow \mathcal{V}$ is via an intermediate flat triangle $\mathcal{Z} \in \mathbb{R}^3$ with vertices $\{\mathbf{Z}^{(p)}\}_{p=1}^3$. Specifically, the affine relation between a point $\mathbf{k} = [k_1, k_2]^{\text{T}} \in \mathcal{K}^{\text{ref}}$ and a point $\mathbf{z} \in \mathcal{Z}$ is

$$\begin{aligned} z_i &= Z_i^{(1)} + \left(Z_i^{(2)} - Z_i^{(1)}\right) k_1 + \left(Z_i^{(3)} - Z_i^{(1)}\right) k_2 \\ &= Z_i^{(1)} + D_{ij} k_j \ , \end{aligned} \tag{50}$$

where $D \coloneqq \left(\left(\mathbf{Z}^{(2)} - \mathbf{Z}^{(1)}\right), \left(\mathbf{Z}^{(3)} - \mathbf{Z}^{(1)}\right)\right) \in \mathbb{R}^{3\times 2}$. The bijection between $\mathbf{z}$ and $\mathbf{\Omega} \in \mathcal{V}$ is

$$\mathbf{\Omega} = \frac{1}{z}\mathbf{z} \ , \tag{51}$$

where $z \coloneqq ||\mathbf{z}||_2 = \sqrt{\mathbf{z} \cdot \mathbf{z}}$, as illustrated in figure 7. Obviously the vertices of $\mathcal{Z}$ must satisfy $\mathbf{V}^{(i)} = \left|\left|\mathbf{Z}^{(i)}\right|\right|_2^{-1} \mathbf{Z}^{(i)}$. Such a bijection between $\mathcal{K}^{\text{ref}}$ and $\mathcal{V}$ allows one to define an angular basis functions in terms of a local variable $\mathbf{k} \in \mathcal{K}^{\text{ref}}$, such as for the octa-functions in equation 17.

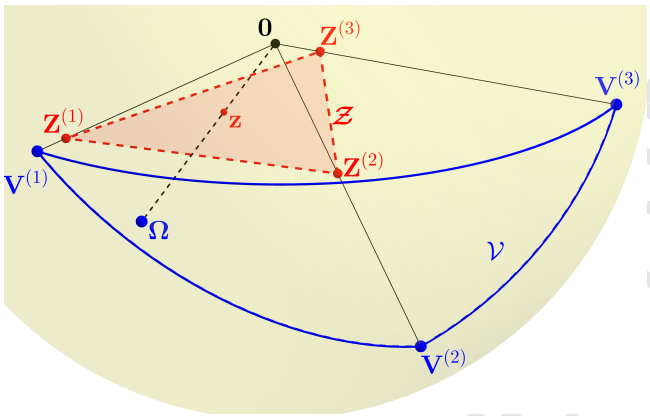

Figure 7: A flat triangle $\mathcal{Z}$ with a corresponding spherical triangle $\mathcal{V}$.

A.2 Spherical gradient of octa-functions

In this section we derive the spherical gradient of a function $g = g(\mathbf{k})$ that is defined in terms of the local coordinate $\mathbf{k}$. We provide an explicit expression for $\partial z_j/\partial\Omega_i$ and $\partial k_j/\partial z_i$ in the equation

$$\partial_i^s g = (\delta_{im} - \Omega_i\Omega_m)\,\frac{\partial z_n}{\partial\Omega_m}\,\frac{\partial k_q}{\partial z_n}\,\frac{\partial g}{\partial k_q}\ . \tag{52}$$

From equation 51,

$$\frac{\partial\Omega_j}{\partial z_i} = \frac{1}{z}\,(\delta_{ij} - \Omega_i\Omega_j)\ , \tag{53}$$

and so $(\partial\Omega_j/\partial z_i)\Omega_j = 0$, which implies that the matrix with coefficients $\partial\Omega_j/\partial z_i$ is singular. Therefore the inverse Jacobian $\partial z_j/\partial\Omega_i$ cannot be obtained in the usual manner. That is,

$$\frac{\partial z_m}{\partial\Omega_i}\frac{\partial\Omega_j}{\partial z_m} \neq \delta_{ij} \neq \frac{\partial\Omega_m}{\partial z_i}\frac{\partial z_j}{\partial\Omega_m}\ , \tag{54}$$

which is a consequence of the fact that $\mathbf{\Omega}$ and $\mathbf{z}$ are constrained. Equation 51 is inverted instead. Let $\mathbf{n}$ be a normal of $\mathcal{Z}$, so that $\mathrm{dist}(\mathcal{Z},\mathbf{0}) = \mathbf{n}\cdot\mathbf{z} = \mathbf{n}\cdot\mathbf{Z}^{(i)}$ is constant for all $\mathbf{z}\in\mathcal{Z}$. Take an inner product of equation 51 with $\mathbf{n}$ to obtain

$$z_j = \frac{\mathrm{dist}(\mathcal{Z},\mathbf{0})}{\mathbf{\Omega}\cdot\mathbf{n}}\Omega_j\ . \tag{55}$$

It follows that

$$\frac{\partial z_j}{\partial\Omega_i} = \frac{\mathrm{dist}(\mathcal{Z},\mathbf{0})}{\mathbf{\Omega}\cdot\mathbf{n}}\left(\delta_{ij} - \frac{1}{\mathbf{\Omega}\cdot\mathbf{n}}\,n_i\Omega_j\right). \tag{56}$$

Note that

$$\Omega_m\frac{\partial}{\partial\Omega_m}z_i = 0\ , \tag{57}$$

as one would expect geometrically.

There are two degrees of freedom in $\mathcal{K}^{\text{ref}}$ and three equations in 50, so we can solve for $\mathbf{k}$ in several nonequivalent ways, the most convenient of which is to left-multiply by $(D^\intercal D)^{-1}D^\intercal \in \mathbb{R}^{2\times 3}$. ($D^\intercal D$ is always invertible, because $\mathcal{Z}$ is nonsingular.) This yields

$$k_j = \left((D^\intercal D)^{-1}D^\intercal\right)_{ji}\left(z_i - Z_i^{(1)}\right) \ . \tag{58}$$

The advantage of this particular representation is that the derivative with respect to $\mathbf{z}$ becomes straightforward:

$$\frac{\partial k_j}{\partial z_i} = \left((D^\intercal D)^{-1}D^\intercal\right)_{ji} = \left(D(D^\intercal D)^{-1}\right)_{ij} . \tag{59}$$

Interestingly, this is not a unique solution: given a displacement $\mathrm{d}z_i$, there are infinitely many matrices $\partial k_j/\partial z_i$ with which the resulting displacements $\mathrm{d}k_j = (\partial k_j/\partial z_i)\ \mathrm{d}z_i$ can be computed correctly. This is because D doesn't have full row rank, which in turn results from the fact that equation 50 is overdetermined if $\mathbf{k}$ is the unknown. The matrices $\partial k_j/\partial z_i$ give different values for $(\partial k_j/\partial z_i)n_i$, which, due to the constraint $\mathbf{z} \in \mathcal{Z} \Rightarrow \mathbf{n}\cdot\mathrm{d}\mathbf{z} = 0$, is inconsequential for the following results.

Substituting equations 56, 57 and 59 in 52, we find

$$\partial_i^s g = \frac{\mathrm{dist}(\mathcal{Z},\mathbf{0})}{\boldsymbol{\Omega}\cdot\mathbf{n}}\left(\delta_{im} - \frac{1}{\boldsymbol{\Omega}\cdot\mathbf{n}}\ n_i\Omega_m\right)\left(D(D^\intercal D)^{-1}\right)_{mn}\frac{\partial}{\partial k_n}\ g \ . \tag{60}$$

This can be simplified for the octa-functions described in section 2.2.1. The vertices $\mathbf{Z}^{(i)}$ are in the same octant and on the octahedron, so that the normal of $\mathcal{Z}$ has components $n_i = (1/\sqrt{3})\ \mathrm{sign}(z_i) = (1/\sqrt{3})\ \mathrm{sign}(\Omega_i)$. This implies $\mathrm{dist}(\mathcal{Z},\mathbf{0}) = 1/\sqrt{3}$ and $\mathbf{n}\cdot\boldsymbol{\Omega} = |||\boldsymbol{\Omega}||_1/\sqrt{3}$. Also, $||\boldsymbol{\Omega}||_1 = 1/z$. The spherical gradient becomes

$$\partial_i^s \Psi_j = \frac{1}{z}\left(\delta_{im} - \mathrm{sign}(z_i)z_m\right)\left(D(D^\intercal D)^{-1}\right)_{mn} C_{jq}\frac{\partial b_q}{\partial k_n} \ , \tag{61}$$

where we used equation 11.

References

[1] Douglas N. Arnold, Franco Brezzi, Bernardo Cockburn, and L. Donatella Marini. Unified analysis of discontinuous Galerkin methods for elliptic problems. *SIAM J. NUMER. ANAL*, pages 1749—-1779, 2001.

[2] J. St. Aubin, A. Keyvanloo, and B. G. Fallone. Discontinuous finite element space-angle treatment of the first order linear Boltzmann transport equation with magnetic fields: Application to MRI-guided radiotherapy. *Medical Physics*, 43(1):195–204, 2016.

[3] Y. Azmy and E. sartori, editors. *Nuclear Computational Science: A Century in Review*. Springer, 2010. ISBN 978-9048134106.

[4] N. Boal, V. Domínguez, and F.-J. Sayas. Asymptotic properties of some triangulations of the sphere. *Journal of Computational and Applied Mathematics*, 211(1):11–22, 2008. ISSN 03770427. doi: 10.1016/j.cam.2006.11.012.

[5] Christoph Börgers and Edward W. Larsen. Asymptotic Derivation of the Fermi Pencil-Beam Approximation. *Nucl. Sci. and Eng.*, 123:343–357, 1995.

[6] Christoph Börgers and Edward W. Larsen. On the accuracy of the Fokker-Planck and Fermi pencil beam equations for charged particle transport. *Medical Physics*, 23(10):1749, 1996.

[7] Paul Castillo. A review of the Local Discontinuous Galerkin (LDG) method applied to elliptic problems. *Applied Numerical Mathematics*, 56(10-11): 1307–1313, oct 2006. ISSN 01689274. doi: 10.1016/j.apnum.2006.03.016.

[8] Andreas Dedner, Pravin Madhavan, and Björn Stinner. Analysis of the discontinuous Galerkin method for elliptic problems on surfaces. *IMA Journal of Numerical Analysis*, 2013. doi: 10.1093/imanum/drs033.

[9] Daniele A. Di Pietro. Cell centered Galerkin methods for diffusive problems. *ESAIM: Mathematical Modelling and Numerical Analysis*, 46(1):111–144, jan 2012. ISSN 0764-583X. doi: 10.1051/m2an/2011016.

[10] Clifton R. Drumm, Wesley C. Fan, Leonard Lorence, and Jennifer Liscumpowell. An Analysis of the Extended-Transport Correction with Application to Electron Beam Transport. *Nuclear Science and Engineering*, 155: 355–366, 2007.

[11] Gerhard Dziuk and Charles M. Elliott. Finite element methods for surface PDEs. *Acta Numerica*, 22(April 2013):289–396, 2013.

[12] Yekaterina Epshteyn and Béatrice Rivière. Estimation of penalty parameters for symmetric interior penalty Galerkin methods. *Journal of Computational and Applied Mathematics*, 206(2):843–872, 2007. ISSN 03770427. doi: 10.1016/j.cam.2006.08.029. URL `http://linkinghub.elsevier.com/retrieve/pii/S0377042706005279`.

[13] Christophe Geuzaine and J F Remacle. Gmsh: A 3-D finite element mesh generator with built-in pre-and post-processing facilities. *International Journal for Numerical Methods in Engineering*, 79(11):1309–1331, 2009. ISSN 1097-0207. doi: 10.1002/nme.

[14] József Kópházi and Danny Lathouwers. A space-angle DGFEM approach for the Boltzmann radiation transport equation with local angular refinement. *Journal of Computational Physics*, 297:637–668, 2015. ISSN 00219991. doi: 10.1016/j.jcp.2015.05.031.

[15] D. Lathouwers. Spatially adaptive eigenvalue estimation for the SN equations on unstructured triangular meshes. *Annals of Nuclear Energy*, 38(9):1867–1876, 2011. ISSN 0306-4549. doi: http://dx.doi.org/10.1016/j.anucene.2011.05.013.

[16] D. Lathouwers. Goal-oriented spatial adaptivity for the SN equations on unstructured triangular meshes. *Annals of Nuclear Energy*, 38(6):1373–1381, 2011. ISSN 0306-4549. doi: http://dx.doi.org/10.1016/j.anucene.2011.01.038.

[17] Q.T. Le Gia. Galerkin approximation for elliptic PDEs on spheres. *Journal of Approximation Theory*, 130(2):125–149, oct 2004. ISSN 00219045. doi: 10.1016/j.jat.2004.07.008.

[18] Elmer E. Lewis and Warren F. Miller. *Computational Methods of Neutron Transport*. American Nuclear Society, Illinois, 1st edition, 1993. ISBN 978-0-89448-452-0.

[19] Xinge Li, Guoliang Xu, and Yongjie Jessica Zhang. Localized discrete Laplace-Beltrami operator over triangular mesh. *Computer Aided Geometric Design*, 39:67–82, nov 2015.

[20] Richard J. Mathar. Zernike Basis to Cartesian Transformations. *Serbian Astronomical Journal*, 179(179):107–120, sep 2009. doi: 10.2298/SAJ0979107M.

[21] J. E. Morel. Fokker-Planck Calculations Using Standard Discrete Ordinates Transport Codes. *Nuclear Science and Engineering*, 79:340–356, 1981.

[22] J. E. Morel, A. Prinja, J. M. McGhee, T. A. Wareing, and B. C. Franke. A discretization scheme for the three-dimensional angular Fokker-Planck operator. *Nuclear Science and Engineering*, 156(2):154–163, 2007. ISSN 00295639.

[23] H. Paganetti, editor. *Proton Therapy Physics*. CRC Press, 2011. ISBN 978-1439836446.

[24] Daniele Antonio Di Pietro and Alexandre Ern. *Mathematical Aspects of Discontinuous Galerkin Methods*. Springer, 2012. ISBN 9783642229800. doi: 10.1007/978-3-642-22980-0.

[25] Richard Sanchez and Jean Ragusa. On the Construction of Galerkin Angular Quadratures. *Nuclear Science and Engineering*, 169:133–154, 2011.

[26] Khosro Shahbazi. An explicit expression for the penalty parameter of the interior penalty method. *Journal of Computational Physics*, 205(2):401–407, may 2005. ISSN 00219991. doi: 10.1016/j.jcp.2004.11.017.

[27] Bruno Turcksin, Jean C. Ragusa, and Jim E. Morel. Angular Multigrid Preconditioner for Krylov-Based Solution Techniques Applied to the Sn Equations with Highly Forward-Peaked Scattering. *Transport Theory and Statistical Physics*, 41(1-2):1–22, 2012. ISSN 0041-1450. doi: 10.1080/00411450.2012.672944.

[28] James S. Warsa, Todd A. Wareing, and Jim E. Morel. Krylov Iterative Methods and the Degraded Effectiveness of Diffusion Synthetic Acceleration for Multidimensional Sn Calculations in Problems with Material Discontinuities. *Nuclear Science and Engineering*, 147:218–248, 2004. doi: 10.13182/NSE02-14.

[29] Guoliang Xu. Discrete Laplace-Beltrami operators and their convergence. *Computer Aided Geometric Design*, 21:767–784, 2004. doi: 0-7695-2078-2.